

# Area-Efficient Three Axis MEMS Lorentz Force Magnetometer

Vashwar Tajdidur Rouf, Mo Li, and David A. Horsley, *Member, IEEE*

**Abstract**—A micro-electromechanical-systems (MEMS) three-axis Lorentz force magnetometer based on a  $0.24 \times 0.4 \text{ mm}^2$  MEMS resonator that is the smallest Lorentz force sensor reported to date is presented in this paper. A magnetic field can be detected in two axes using a single MEMS structure. Placing two structures perpendicular to each other in a single die makes three-axis sensing possible. Sensing is performed by exciting the MEMS resonator at its in-plane and out-of-plane mechanical resonant frequencies of 40.5 and 107.4 kHz, respectively. A modest die-level vacuum packaging results in in-plane and out-of-plane mechanical quality factors of 110 and 310, respectively. The sensor has a bandwidth of 184 Hz for  $z$ -axis and 189 Hz for  $x/y$ -axis magnetic field. With an excitation power of 2 mW, the sensor resolution is 285 nT/ $\sqrt{\text{Hz}}$  for  $z$ -axis magnetic field inputs and 344 nT/ $\sqrt{\text{Hz}}$  for  $x/y$ -axis magnetic field inputs. The resolution is limited by Brownian noise in the  $z$ -axis whereas the  $x/y$ -axis resolution is limited by electronic noise. With an averaging time of 288 s, the sensor shows an offset stability of 23 nT.

**Index Terms**—Magnetic sensors, magnetometers, MEMS resonators, navigation.

## I. INTRODUCTION

WITH personal electronic devices like cell phones and tablets having more functionality, the market for low cost MEMS sensors is growing rapidly. The need for inclusion of an electronic compass in such devices to facilitate navigation and location based services has dramatically increased the demand for MEMS and magnetic sensors. Magneto-resistive (MR) and Hall-effect sensors are the dominant technologies in existing electronic compasses. Hall-effect sensors have advantages over MR sensors as they do not require any specialized magnetic material while MR sensors are more sensitive than Hall-effect sensors. A representative MR sensor, the HMC5883L, has a resolution (noise-equivalent magnetic field) of 500 nT [2], while a typical Hall-effect sensor, the AK8975 of AKM semiconductor, has a 300 nT resolution [3]. Using 10  $\mu\text{T}$  as a conservative estimate for Earth's field, the

Manuscript received February 13, 2013; revised April 17, 2013; accepted May 9, 2013. Date of publication May 23, 2013; date of current version October 2, 2013. This work was supported in part by the U.S. National Science Foundation CAREER under Award CMMI-0846379. The associate editor coordinating the review of this paper and approving it for publication was Prof. Eh Yang.

V. T. Rouf and M. Li are with the Department of Electrical and Computer Engineering, University of California, Davis, CA 95616 USA (e-mail: vtrouf@ucdavis.edu; moxli@ucdavis.edu).

D. A. Horsley is with the Department of Mechanical and Aerospace Engineering, University of California, Davis, CA 95616 USA (e-mail: dahorsley@ucdavis.edu).

Color versions of one or more of the figures in this paper are available online at <http://ieeexplore.ieee.org>.

Digital Object Identifier 10.1109/JSEN.2013.2264807

TABLE I  
LORENTZ FORCE MAGNETOMETERS

Publication	AXIS	Area (mm <sup>2</sup> )	Current (mA)	Power (mW)	Resolution (nT/ $\sqrt{\text{Hz}}$ )
This paper	Z	0.096	4.5	2	285
[1]	X/Y		4.5	2	344
Li <i>et al.</i> [4]	Z	0.2	0.4	0.46	137
	X/Y		0.2	0.14	440
Kyynarainen <i>et al.</i> [5]	X/Y	1.96	0.1	Not Reported	10
	Z		0.1	Not Reported	70
Thompson <i>et al.</i> [6]	Z	2.8	2.67	1.8	87
Herrera-May <i>et al.</i> [7]	X/Y		22	10	140
Emmerich <i>et al.</i> [8]	Z	0.78	0.93	Not Reported	200
Kadar <i>et al.</i> [9]	X/Y		30	Not Reported	2.4*
Alandry <i>et al.</i> [10]	X/Y	0.23	4.5**	Not Reported	258
Tapia <i>et al.</i> [11]	X/Y		10	2.05	80

\*Theoretical estimate. Measured value is not reported.

\*\* Current includes detection electronics.

AK8973 and HMC5883 have compass heading accuracies of 1.7 and 2.8 degrees respectively.

Lorentz force sensors share the same advantages of Hall-effect sensors over MR sensors. Compared to Lorentz force sensors, Hall-effect sensors have lower sensitivity to magnetic field. Hall-effect sensors also need magnetic concentrators to sense field parallel to the device. Lorentz force sensors are free from this limitation. MEMS Lorentz sensors have the additional advantage of easy integration with MEMS gyroscopes and accelerometers currently used in consumer electronics. A summary of previous Lorentz force magnetometers is presented in Table I. Most of the previous magnetometers were single-axis sensors, had power consumption of several mW, and require fabrication steps not available in a standard inertial sensor fabrication process. A metric for comparing these sensors is the resolution achieved at a given power consumption. However, power consumption is not provided in many previous papers so we include only the excitation current in the table.

In comparison to an earlier two-axis sensor [4], the sensor presented here requires less than half the area and has similar noise-equivalent magnetic field (measured in nT/ $\sqrt{\text{Hz}}$ ). Using a more modest vacuum seal (20 mbar) makes the device described in this paper more compatible with accelerometer co-fabrication and results in an order-of-magnitude lower

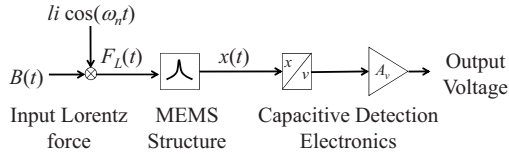


Fig. 1. Sensor block diagram. Sinusoidal drive currents modulate field signals  $B(t)$  to produce force  $F_L(t)$  centered around the in-plane and out-of-plane natural frequencies. The resulting force creates displacement which is detected using a capacitive measurement scheme.

quality factor ( $Q$ ), providing a fast time-response and greater bandwidth ( $>100$  Hz versus  $<10$  Hz in [4]). The sensor presented here uses single crystal silicon as the device layer whose resistivity is much lower than our previous work. Lower resistivity of the device layer has made it possible to scale down the size of the sensor and still achieve good performance with reasonable power consumption. Our previous sensor also suffered from large parasitic motion resulting from electrostatic force due to high (5.9 k $\Omega$ ) resistance and mismatch of the flexure resistances. Reducing and matching the resistance of the flexures has eliminated this parasitic electrostatic motion in the current device.

## II. SENSOR DESIGN AND MODELING

Fig. 1 illustrates the working principle of the sensor, which is similar to a multi-axis accelerometer. Lorentz force is generated when an external magnetic field interacts with a current-carrying silicon MEMS structure. This Lorentz force moves the mechanical structure and capacitive sensing is used to detect the resulting motion. To increase the sensitivity, the sensor is excited at its mechanical resonance frequency using an AC current. As a result, the field induced motion will be amplified by the quality factor ( $Q$ ) of the resonator. This frequency selective detection scheme also reduces sensitivity due to acceleration and cross axis magnetic field.

Fig. 2 shows a SEM image of the sensor. The z-axis magnetic field creates in-plane (x- or y-axis) motion which is sensed using electrodes placed inside the MEMS structure. The x/y- axis magnetic field creates an out-of-plane (z-axis) motion which is detected using a metal electrode laid underneath the suspended MEMS structure. The sensor structure is fabricated from a 10  $\mu\text{m}$  thick layer of single crystal silicon using a standard inertial sensor fabrication process. A metal layer beneath the silicon MEMS structure is used for electrical interconnect and to form electrodes for sensing the structure's out-of-plane motion. A wafer-level vacuum encapsulation is performed by sealing a second wafer to the MEMS wafer using eutectic bonding, resulting in a sealed pressure of approximately 20 mbar. For testing purposes, the sensor dice are wire bonded to a small printed circuit board (PCB) containing the excitation and capacitive sensing electronics. Detailed design parameters are presented in Table II.

### A. Magnetic Sensitivity

Interaction of a current carrying wire with magnetic field generates Lorentz force. This force ( $F_L$ ) depends on the

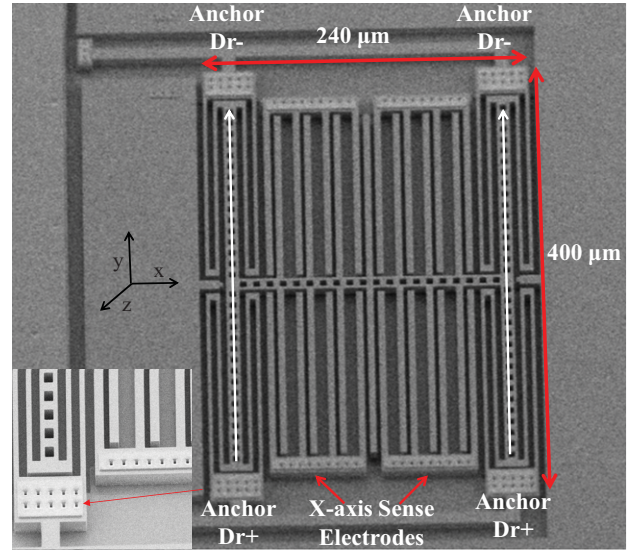


Fig. 2. SEM image of the silicon sensor structure. White arrows indicate the flexure current. The z-axis sensing capacitor is located beneath the structure. Inset: magnified image of the anchor of the MEMS structure.

TABLE II  
DEVICE PARAMETERS

Parameter	VALUE	Units
Device Thickness	10	$\mu\text{m}$
Area	0.096	$\text{mm}^2$
Spring Constant (in-plane), $k_x$	31	N/m
Spring Constant (out-of-plane), $k_z$	137	N/m
Quality Factor (in-plane), $Q_x$	110	-
Quality Factor (out-of-plane), $Q_z$	300	-
Capacitance (in-plane)	49	fF
Capacitance (out-of-plane)	118.9	fF
Capacitive gap (in-plane)	2.14	$\mu\text{m}$
Capacitive gap (out-of-plane)	2.85	$\mu\text{m}$
Natural Frequency (in-plane), $f_{n,x}$	40.5	kHz
Natural Frequency (out-of-plane), $f_{n,z}$	107.4	kHz
Resistance	98	$\Omega$
Effective Length, $L_e$ (in-plane)	180	$\mu\text{m}$
Effective Length, $L_e$ (out-of-plane)	150	$\mu\text{m}$

magnetic field ( $B$ ), current ( $i$ ) and length of the wire ( $L$ )

$$F_L = Li \times B \quad (1)$$

The force is perpendicular to the direction of both current flow and magnetic field. Although the current carrying flexure of our sensor is not a straight wire, an effective flexure length ( $L_e$ ) can be computed using finite element method (FEM) analysis [5] to apply (1).

The MEMS structure was designed to move in two axes to facilitate two-axis magnetic field measurement using a single structure. The force to displacement transfer function for each axis is that of a simple harmonic oscillator:

$$H(f) = \frac{1}{k} \frac{f_n^2}{(f_n^2 - f^2) + jQ^{-1}ff_n} \quad [\text{m/N}] \quad (2)$$

where  $k$  is the stiffness of mechanical structure,  $f$  is frequency,  $Q$  and  $f_n$  are the quality factor and frequency of the resonance. To distinguish in-plane and out-of-plane motion these three parameters are identified using the subscripts  $x$  and  $z$  in the rest of this paper.

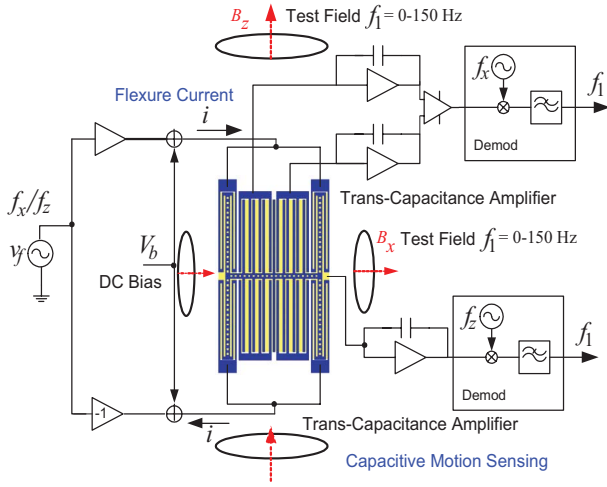


Fig. 3. Test circuitry for device characterization. A common mode dc bias voltage  $V_b$  is used for capacitive sensing. In-plane motion is sensed using a differential trans-capacitance amplifier. Out-of-plane motion is sensed using a single trans-capacitance amplifier connected to the electrode beneath the structure (indicated in yellow).

An external DC magnetic field interacting with an AC excitation current at  $f_n$  will create motion at the natural frequency of the device. Using (1) and (2), the mechanical field sensitivity is given as:

$$S_{XB} = L_e i |H(f_n)| = L_e i Q/k \quad [\text{m/T}] \quad (3)$$

The setup for electrical characterization of the sensor is shown in Fig. 3. Generation of excitation signals and demodulation of output voltage was done using a lock in amplifier, while the rest of the electrical circuit is implemented in a printed circuit board (PCB). The use of a PCB results in large parasitic capacitance which in turn increases the electronic noise of the system. It is shown later that increase of electronic noise prevents achieving Brownian noise limited performance for  $x/y$ -axis field sensing.

Excitation current was generated by applying differential voltage across the MEMS flexures. To facilitate capacitive detection, a common mode DC bias voltage  $V_b$  was added to this differential voltage. Fixed capacitive electrodes placed inside and beneath the structure were connected to trans-capacitance amplifiers to convert the motional current to voltage. The small signal displacement-to-voltage sensitivity is given as:

$$S_{VX} = \frac{1}{C_f} \frac{dC}{dx} V_b \approx (C_s/C_f) V_b/g \quad [\text{V/m}] \quad (4)$$

where  $C_s$  is the sense capacitance,  $C_f$  is the feedback capacitance of trans-capacitance amplifier and  $g$  is the capacitive air gap.

Field sensitivity of the magnetic sensor can be computed by combining (3) and (4):

$$S_{VB} = S_{VX} S_{XB} = (C_s/C_f) (V_b/g) L_e i Q/k \quad [\text{V/T}] \quad (5)$$

Z-axis field creates in-plane motion that is sensed using a pair of differential motion-sensing capacitors  $C_{s+}$  and  $C_{s-}$ .

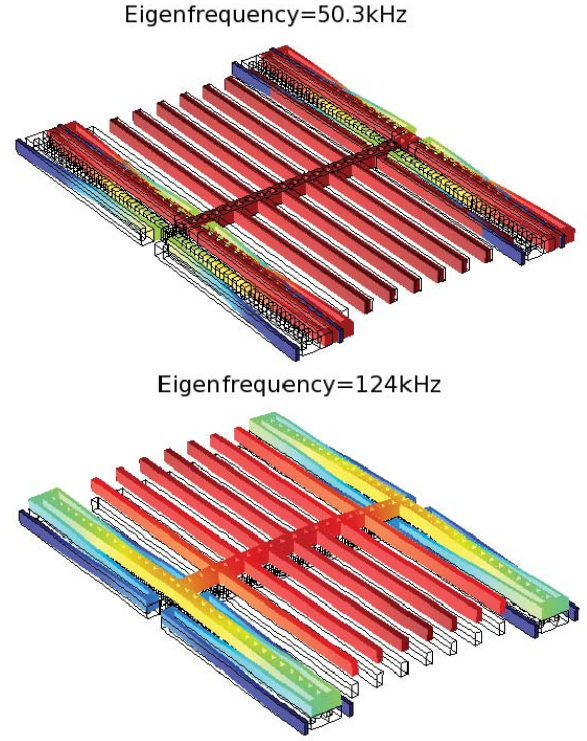


Fig. 4. FEM mode shapes for in-plane (top) and out-of-plane motion (bottom) simulated using COMSOL software.

The differential measurement of these two capacitors results in twice the signal level and sensitivity to z-axis field is twice the value computed from (5).

### B. FEM Analysis

FEM analysis was performed using COMSOL Multiphysics software to calculate the natural frequency and vibration mode shapes of the mechanical structure. Fig. 4 shows the in-plane and out-of-plane mode shapes of the sensor. The natural frequency of the in-plane and the out-of-plane motion of the structure is 50.3 kHz and 124.0 kHz respectively. FEM analysis shows that the mechanical structure has an undesirable rocking mode at 113 kHz. Since this mode is far away from the in-plane and out-of-plane natural frequencies, it does not have any effect on the performance of the sensor. The stiffness of the structure in each axis ( $k_x$  and  $k_z$ ) was calculated by applying a test force and measuring the displacement using COMSOL. The procedure to calculate effective flexure length  $L_e$  using FEM has been discussed in detail in our previous work [4]. In brief, the Lorentz force at a given current and magnetic field was simulated by applying a distributed force to the mechanical structure. The effective length was then computed from the resulting displacement of the mechanical structure and the previously derived stiffness value.

### C. Noise

Noise in the output of the sensor comes from two sources, Brownian (thermo-mechanical) noise and electronic noise from the detection electronics. Both of these are white noise sources as the measurement is performed well above the

sensor's  $1/f$  corner frequency, which is  $\sim 500$  Hz for our current setup. The Brownian noise density is given by

$$F_B = \sqrt{4k_b T \frac{k}{2\pi f_n Q}} [N/\sqrt{Hz}] \quad (6)$$

Where  $k_b$  is Boltzmann's constant,  $T$  is the temperature in degrees Kelvin, and  $k$  is the spring constant.

The electronic noise density at the output of trans-capacitance amplifier comes from the following three sources:

1) Amplifier input-referred voltage noise:

$$vn_1 = vn_i \left(1 + \frac{C_T}{C_f}\right) [V/\sqrt{Hz}] \quad (7)$$

where  $vn_i$  is the inputreferred noise of the op-amp,  $C_T$  is total capacitance to ground at the input of the opamp and  $C_f$  is the feedback capacitance. The input capacitance of amplifier and stray capacitance from PCB are the main sources of  $C_T$ . Input-referred voltage noise is the dominant source of electronic noise in the trans-capacitance amplifier.

ii) Amplifier input noise current:

$$vn_2 = in_i \frac{R_f}{1 + j\omega R_f C_f} [V/\sqrt{Hz}] \quad (8)$$

where  $in_i$  is the inputreferred noise current and  $R_f$  is the feedback resistance of the transcapacitance amplifier.

iii) Current noise from feedback resistor:

$$vn_3 = \left(\sqrt{\frac{4k_b T}{R_f}}\right) \frac{R_f}{1 + j\omega R_f C_f} [V/\sqrt{Hz}] \quad (9)$$

The total electronic noise is given by

$$vn = \sqrt{vn_1^2 + vn_2^2 + vn_3^2} [V/\sqrt{Hz}] \quad (10)$$

The electronic noise computed using (10) is  $175$  nV/ $\sqrt{Hz}$ , while measured electronic noise at the output of the trans-capacitance amplifier is  $315$  nV/ $\sqrt{Hz}$ . Since in-plane motion is sensed differentially, for z-axis field the electronic noise floor is further increased by a factor of  $\sqrt{2}$ .

Near the operating frequency  $f_n$ , the equivalent input force resulting from electronic noise is

$$F_e = vn (S_{VX} |H(f_n)|)^{-1} [N/\sqrt{Hz}] \quad (11)$$

The total force noise of the sensor is given as

$$F = \sqrt{F_B^2 + F_e^2} [N/\sqrt{Hz}] \quad (12)$$

while the theoretical resolution of the sensor is given as

$$B = F / (L_e i) [T/\sqrt{Hz}] \quad (13)$$

Brownian noise is the fundamental limit for a Lorentz force sensor. Achieving this limit requires lowering the electronic noise,  $F_e$ . One way to reduce  $F_e$  is to increase the DC bias (thereby increasing  $S_{VX}$ ). To make the Brownian noise equal to the electronic noise, a DC bias of  $13$  V would be needed in the z-axis and  $42$  V would be needed in the x/y-axis.

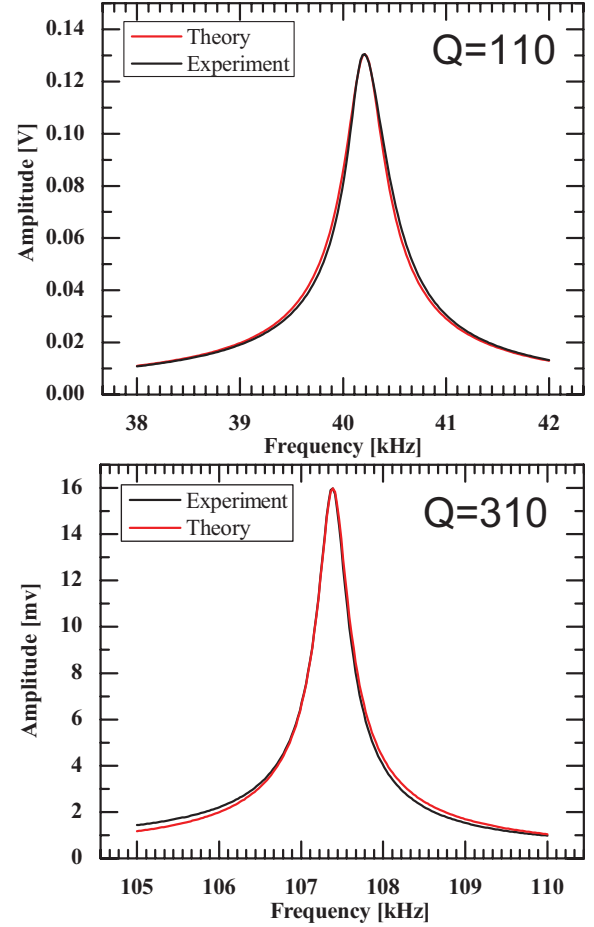


Fig. 5. Frequency response of the in-plane (top) and out-of-plane (bottom) vibration modes.

### III. EXPERIMENTAL RESULTS

#### A. Frequency Response

The amplitude of signal voltage from the sensor as a function of excitation-current frequency was measured using a digital lock in amplifier (Zurich Instruments HF2LFI) to generate excitation signals and to record and demodulate the sensor's output voltage. Using a DC bias of  $15$  V and an excitation power of  $2$  mW, the frequency response of the in-plane and the out-of-plane motion of the sensor was measured by sweeping the frequency of the excitation current. The measured frequency responses, shown in Fig. 5, were fit with a second-order transfer function (2), yielding  $f_n = 40.5$  kHz,  $Q = 110$  for in-plane and  $f_n = 107.4$  kHz,  $Q = 310$  for out-of-plane motion.

The measured 3 dB bandwidth is  $184$  Hz for z-axis field and  $189$  Hz for x/y-axis field. Measured natural frequencies are very close to the frequencies predicted by FEM analysis, which were  $50.3$  kHz and  $124.0$  kHz for the in-plane and the out-of-plane modes, respectively. The slight difference between experimental and theoretical values can be attributed to line-width reduction during the fabrication process.

To measure the vacuum level in the encapsulated sensor, the vacuum seal was broken on a representative device and the frequency response was measured at different pressures in



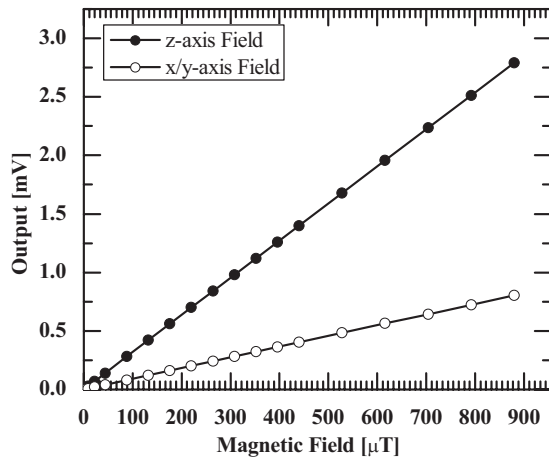


Fig. 6. Measured magnetic transfer characteristic of the sensor. Sensitivity for z-axis field is 3.2 V/T and for x/y-axis field is 0.92 V/T.

a vacuum chamber. The  $Q$  of the sensor at 20 mbar matches with the  $Q$  of the encapsulated sensor.

### B. Magnetic Sensitivity

AC magnetic fields in the range from 10  $\mu$ T to 880  $\mu$ T were applied to measure the sensitivity of the sensor. To separate the magnetic test signal from capacitive feed-through and any stray DC magnetic fields, measurements were conducted using a sinusoidal field input. These measurements were performed using DC bias of 15 V and excitation current power of 2 mW. Fig. 6 shows the transfer characteristic of the sensor. The measured dc sensitivity is 3.2 V/T for z-axis field and 0.92 V/T for x/y-axis field. The measured values are very close to values computed from (5) which are 3.3 V/T for z-axis field and 1.01 V/T for x/y-axis field. The sensitivity is lower in the x/y axis due to the use of single-ended sensing as well as differences in stiffness, effective flexure length, sense capacitance, and quality factor between the two vibration modes. It is also evident from Fig. 6 that the sensor is linear for the entire measurement range (10  $\mu$ T to 880  $\mu$ T). Since our target application requires measuring Earth's magnetic field and the sensor exhibits linear behavior measuring magnetic field an order of magnitude higher than Earth's field, the sensor is suitable for use for navigation purposes.

### C. Sensor Noise and Field Resolution

Fig. 7 shows the amplitude of the voltage response as a function of the frequency of the excitation current of each axis in response to a 44  $\mu$ T 10 Hz magnetic field input. A DC bias of 15 V and excitation power of 2 mW was used for this measurement. At these operating conditions, z-axis spot noise is 912 nV/ $\sqrt{\text{Hz}}$  which corresponds to a magnetic field resolution of 285 nT/ $\sqrt{\text{Hz}}$ . For x/y-axis field, the electronic noise floor is 315 nV/ $\sqrt{\text{Hz}}$  which corresponds to a field resolution of 344 nT/ $\sqrt{\text{Hz}}$ . In each spectrum, the central peak at  $f_n$  occurs due to feedthrough of the excitation signal into the capacitive sensing channel. The feedthrough is partially cancelled by the differential signal path employed in the z-axis and as a result the central peak is smaller in this measurement. In an ASIC implementation, capacitive feedthrough is often

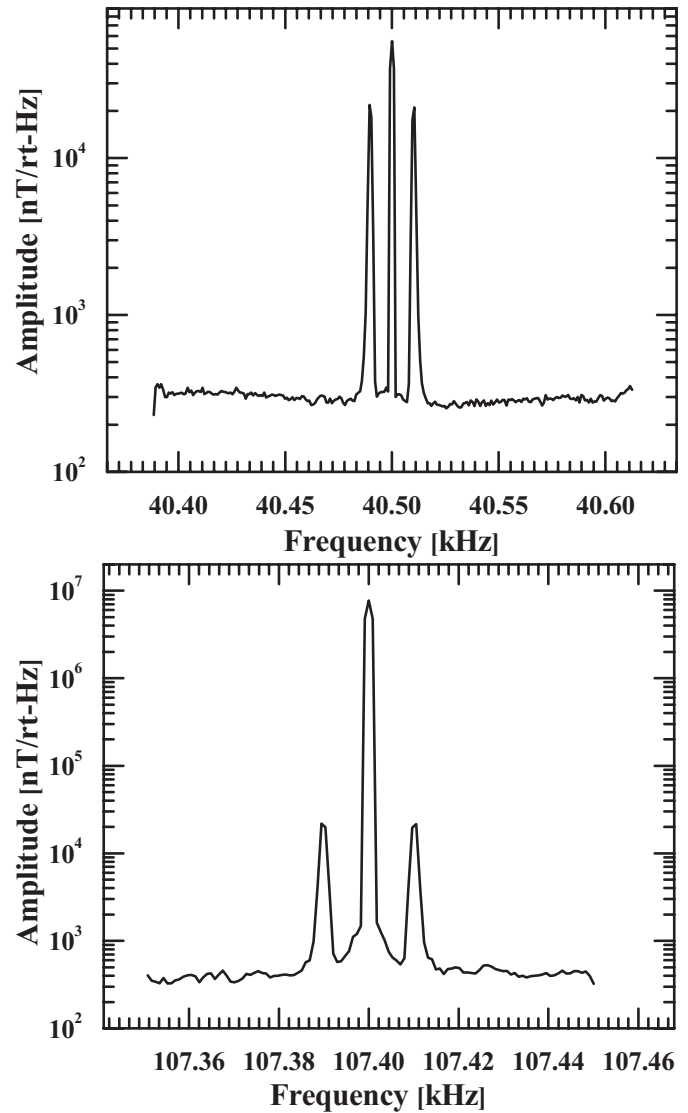


Fig. 7. Amplitude of the voltage response as a function of the frequency of the excitation current for z-axis field (top) and x/y-axis field (bottom) with a dc bias of 15 V, driving power of 2 mW and a 44  $\mu$ T 10 Hz ac magnetic field.

cancelled using on-chip compensation capacitors [12]. Any remaining feedthrough appears as a constant offset when measuring DC magnetic fields. Measurements of the offset stability of the sensor (Section E) show that the offset stability is adequate even with the relatively large level of feedthrough shown here.

A close-up of the output noise spectrum in the z-axis is shown in Fig. 8 to illustrate that the output is dominated by Brownian noise. This measurement was collected with zero excitation current, thereby setting the magnetic sensitivity to zero and assuring that the output contains only Brownian and electronic noise. The measured noise matches closely with the theoretical value for Brownian noise computed using (6) and (12). The x/y-axis field resolution is limited by electronic noise due to the relatively large stray capacitance present in the detection electronics. Brownian noise-limited performance could be achieved in the x/y axis by lowering the stray capacitance by a factor of three.

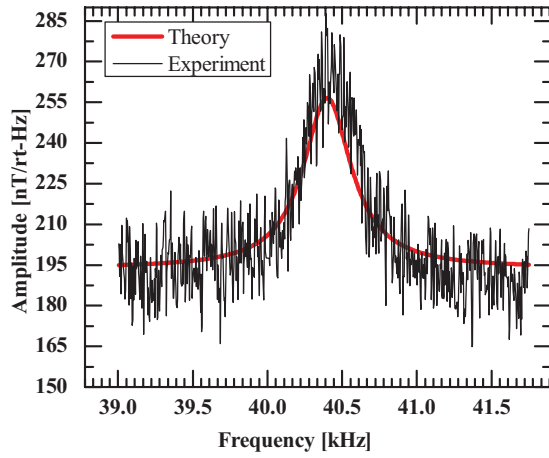


Fig. 8. Output noise spectrum for the z-axis field-sensing channel measured at  $V_b = 15$  V. The output noise is dominated by thermomechanical (Brownian) noise force that is clearly shaped by the sensor's mechanical transfer function.

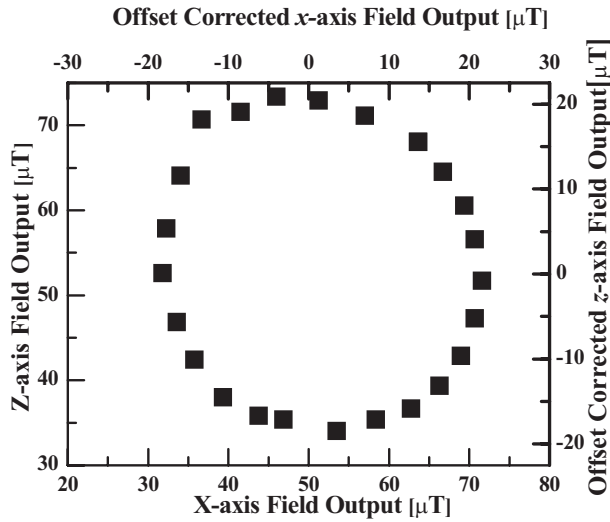


Fig. 9. Change of sensor outputs due to rotation of the sensor. The output was measured with an interval of  $15^\circ$  and a measurement bandwidth of 1 Hz.

#### D. Compass Operation

An experiment was conducted to demonstrate the sensor's ability to operate as a compass. The sensor was mounted on rotation stage and rotated through  $360^\circ$ . The sensor was mounted with the  $x$  and  $z$  axis aligned horizontally. Fig. 9 shows the two outputs of the sensor as it is rotated. The departure of the output from an ideal circle is attributed to the placement error of the sensor on the rotation stage, so that the sensor's  $x/z$  plane was not well-aligned to Earth's field.

To reduce power consumption, most commercial magnetic sensors used in smart-phones and other personal electronic devices usually do not operate in a continuous mode, but are duty-cycled to produce magnetic measurements at approximately 8 samples/s. However, Lorentz force sensors are resonant sensors, and may not be able to operate with a fast on/off duty cycle if the resonator's settling time constant, given by  $\tau = 2Q/f_n$ , is too long. The sensor presented here has a  $Q$  an order of magnitude lower than our previous work and hence a short settling time constant (on the order of 3 ms). Fig. 10 demonstrates duty-cycled operation of the magnetic sensor.

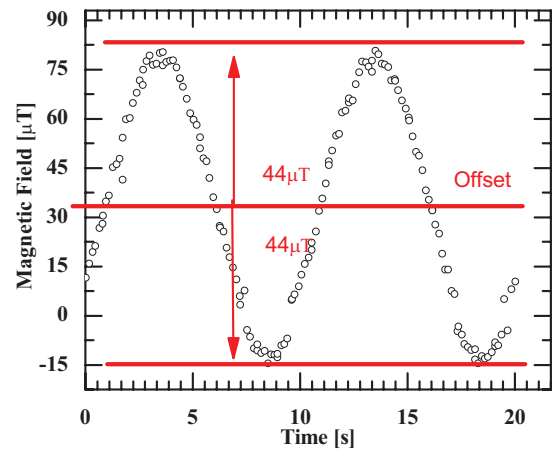


Fig. 10. Demonstration of duty-cycled operation. A 0.1 Hz  $44 \mu\text{T}$  ac magnetic field was applied. The sensor was operated with a driving power of 2 mW at 20% duty cycle. Output was sampled at 8 times per second.

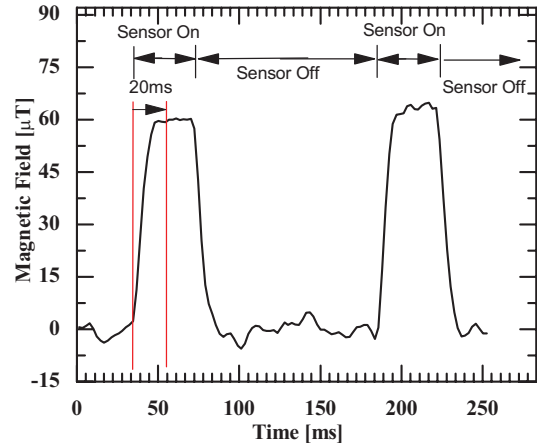


Fig. 11. Demonstration of duty-cycled operation showing sensor response each on/off excitation cycle. The 20 ms settling time matches the expected settling time for a measurement bandwidth of 40 Hz.

The sensor was excited with a peak power of 2 mW at 20% duty-cycle. A  $44 \mu\text{T}$  0.1 Hz AC magnetic field was applied to the sensor. The output was measured with a bandwidth of 40 Hz and sampled 8 times per second. Fig. 11 shows the response for each cycle. The settling time for each cycle is around 20 ms which is in agreement with the settling time of the 40 Hz low-pass filter.

#### E. Offset Stability and Temperature Dependence

Bias, or offset in a magnetic sensor's output, is indistinguishable from a static magnetic field, and results in bias in the compass heading. The Allan deviation of the sensor's output was measured to study the stability of the sensor's bias [13]. Many sources contribute to bias instability including  $1/f$  and  $1/f^2$  noise in the detection circuitry. Fig. 12 shows the measured Allan deviation for a DC bias of 15 V and an excitation power of 2 mW. The sensor has a bias instability of 23 nT with an averaging time of 288 s. This is an order of magnitude lower than our previous work [4] and is attributable to reduced motion due to parasitic electrostatic force at the excitation frequency,  $f$ .

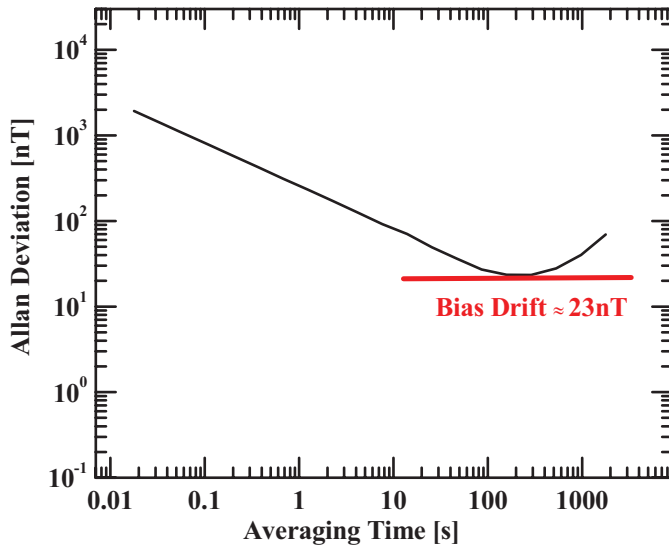


Fig. 12. Measured Allan Deviation for 15V dc Bias. The sensor has a bias instability of 23 nT with 288 s averaging time.

Since the magnetometer presented here is a resonant sensor, temperature changes will affect its performance. Si resonators have a well defined temperature coefficient of frequency of around 30 ppm/°C [14]. Thus, operating the sensor in commercial temperature range (0 °C-85 °C) will result in a maximum variation of natural frequency of 104 Hz for z-axis field sensing and 274 Hz for x/y-axis field sensing. Assuming that the generation of excitation current is insensitive to temperature variation, z-axis field sensing will not be affected by the change of temperature because the resonant frequency variation is much less than the bandwidth of the sensor.

However, for x/y-axis field sensing, the frequency variation is larger than the bandwidth. One solution would be to use an electronically programmable oscillator to adjust the excitation current as a function of temperature to compensate for the resonator's temperature coefficient of frequency.

#### IV. CONCLUSION

This paper has described the smallest Lorentz force MEMS magnetometer reported so far. The MEMS structure has two degrees of freedom, enabling it to measure magnetic field in two axes using a single structure. Key parameters of the sensor are summarized in Table III. With a modest vacuum level of 20 mbar achieved through wafer-level encapsulation, the sensor has a  $Q$  of 110 and 310 for in-plane and out-of-plane motion respectively. The resulting  $Q$  corresponds to a sensor bandwidth of 184 Hz for z-axis and 189 Hz for x/y-axis field. With such a wide bandwidth, the magnetic sensor is suitable to operate in a duty-cycled mode which can significantly reduce power consumption. With an excitation power of 2 mW, the sensor has a z-axis field sensitivity of 3.2 V/T and x/y-axis field sensitivity of 0.92 V/T. Differences in the mechanical properties of the MEMS structure for in-plane and out-of-plane motion contribute to lower sensitivity for x/y-axis magnetic field. The sensor has a resolution of 285 nT/√Hz for z-axis and 344 nT/√Hz for x/y-axis field.

TABLE III  
SUMMARY OF KEY SENSOR PARAMETERS

Parameter	Measured Value	
	X/Y-Axis Field	Z-Axis Field
Bandwidth (Hz)	189	184
Bias Voltage (V)	15	15
Excitation Current (mA)	4.5	4.5
Power (mW)	2	2
Noise (nT/√Hz)	344	285

For z-axis field the sensor is limited by Brownian noise while the x/y-axis field resolution is limited by electronic noise arising from detection electronics. Performance in the x/y-axis can be further improved by reducing stray capacitance in the detection electronics. The sensor performance can also be improved by better vacuum packaging. Better vacuum will result in higher  $Q$  which in turn will lower the noise. For example, a 4x increase in  $Q$  will reduce the Brownian noise by a factor of two, while still maintaining an acceptable bandwidth of 45 Hz. The sensor has a bias instability of 23 nT with an averaging time of 288 s. The performance of this MEMS magnetic sensor is comparable to or better than commercially available Hall-effect and MR magnetic sensors and it is suitable for use in smart-phones and other electronic devices for navigation purposes.

#### ACKNOWLEDGMENT

The authors gratefully acknowledge Taiwan Semiconductor Manufacturing Company (TSMC) for device fabrication.

#### REFERENCES

- [1] V. T. Rouf, M. Li, and D. A. Horsley, "Area-efficient 3-axis micro-mechanical magnetic sensor," in *Proc. IEEE Sensors Conf.*, Oct. 2012, pp. 2054–2057.
- [2] *Three-Axis Digital Compass IC*, HMC5883L datasheet, Honeywell, Inc., Morristown, NJ, USA, Feb. 2013.
- [3] *3-Axis Electronic Compass*, AK8975 datasheet, Asahi Kasei Microdevices Semicond. Inc., Tokyo, Japan, May 2010.
- [4] M. Li, V. T. Rouf, M. J. Thompson, and D. A. Horsley, "Three-axis lorentz-force magnetic sensor for electronic compass applications," *J. Microelectromech. Syst.*, vol. 21, no. 4, pp. 1002–1010, Aug. 2012.
- [5] J. Kyynäräinen, J. Saarilahti, H. Kattelus, A. Kärkkäinen, T. Meinander, A. Oja, P. Pekko, H. Seppä, M. Suhonen, H. Kuisma, S. Ruotsalainen, and M. Tilli, "A 3D micromechanical compass," *Sens. Actuators A, Phys.*, vol. 142, no. 2, pp. 561–568, Apr. 2008.
- [6] M. J. Thompson and D. A. Horsley, "Parametrically amplified z-axis lorentz force magnetometer," *J. Microelectromech. Syst.*, vol. 20, pp. 702–710, Jun. 2011.
- [7] A. L. Herrera-May, P. J. García-Ramírez, L. A. Aguilera-Cortés, J. Martínez-Castillo, A. Saucedo-Carvajal, L. García-González, and E. Figueras-Costa, "A resonant magnetic field microsensor with high quality factor at atmospheric pressure," *J. Micromech. Microeng.*, vol. 19, no. 1, p. 015016, 2009.
- [8] H. Emmerich and M. Schofthaler, "Magnetic field measurements with a novel surface micromachined magnetic-field sensor," *IEEE Trans. Electron Devices*, vol. 47, no. 5, pp. 972–977, May 2000.
- [9] Z. Kádár, A. Bossche, P. M. Sarro, and J. R. Mollinger, "Magnetic-field measurements using an integrated resonant magnetic-field sensor," *Sens. Actuators A, Phys.*, vol. 70, no. 3, pp. 225–232, Oct. 1998.
- [10] B. Alandry, L. Latorre, F. Mailly, and P. Nouet, "A fully integrated inertial measurement unit: Application to attitude and heading determination," *IEEE Sensors J.*, vol. 11, no. 11, pp. 2852–2860, Nov. 2011.

- [11] J. A. Tapia, A. L. Herrera-May, P. J. García-Ramírez, J. Martínez-Castillo, E. Figueras, A. Flores, and E. Manjarrez, "Sensing magnetic flux density of artificial neurons with a MEMS device," *Biomed. Microdevices*, vol. 13, no. 2, pp. 303–313, Apr. 2011.
- [12] J. Seeger, M. Lim, and S. Nasiri, "Development of high-performance, high-volume consumer MEMS gyroscopes," in *Proc. Solid-State Sens., Actuators, Microsyst. Workshop*, 2010, pp. 61–64.
- [13] N. El-Sheimy, H. Hou, and X. Niu, "Analysis and modeling of inertial sensors using Allan variance," *IEEE Trans. Instrum. Meas.*, vol. 57, no. 1, pp. 140–149, Jan. 2008.
- [14] R. Melamud, M. Hopcroft, C. Jha, K. Bongsang, S. Chandorkar, R. Candler, and T. W. Kenny, "Effects of stress on the temperature coefficient of frequency in double clamped resonators," in *Proc. 13th Int. Conf. TRANSDUCERS, Solid-State Sens., Actuators, Microsyst.*, Jun. 2005, pp. 392–395.



**Vashwar T. Rouf** received the B.Sc. degree from the Bangladesh University of Engineering & Technology, Dhaka, Bangladesh, in 2008, and the M.Sc. degree from the University of California, Davis, CA, USA, in 2012, where he is currently pursuing the Ph.D. degree. He was a Lecturer with the Bangladesh University of Engineering & Technology from 2008 to 2010. His current research interests include MEMS inertial sensor and analog integrated circuits.



**Mo Li** received the B.S. degree in microelectronics from Peking University, Beijing, China, in 2011. He completed his undergraduate thesis in the MEMS Lab, University of California, Davis, CA, USA, as an Exchange Student. He is currently a Graduate Student Researcher with the MEMS Lab, University of California. His current research interests include MEMS sensors and analog integrated circuits.



**David A. Horsley** (M'97) received the B.S., M.S., and Ph.D. degrees in mechanical engineering from the University of California, Berkeley, CA, USA, in 1992, 1994, and 1998, respectively.

He is an Associate Professor with the Department of Mechanical and Aerospace Engineering, University of California, Davis, CA, USA, and has been a Co-Director of the Berkeley Sensor and Actuator Center since 2005. Prior to joining the Faculty at UC Davis, he held research and development positions with Dicon Fiberoptics, Hewlett Packard Laboratories, and Onix Microsystems. His current research interests include microfabricated sensors and actuators with applications in optical MEMS, communication, displays, and physical and biological sensors.

Prof. Horsley is a recipient of the NSF CAREER Award and the UC Davis College of Engineering's Outstanding Junior Faculty Award.